

Tuning gravitational-wave detector networks to measure compact binary mergers

Scott A. Hughes*

Kavli Institute for Theoretical Physics, University of California, Santa Barbara, CA 93106

(Dated: November 6, 2018)

Gravitational waves generated by the final merger of compact binary systems depend on the structure of the binary’s members. If the binary contains neutron stars, measuring such waves can teach us about the properties of matter at extreme densities. Unfortunately, these waves are typically at high frequency where the sensitivity of broad-band detectors is not good. Learning about dense matter from these waves will require networks of broad-band detectors combined with narrow-band detectors that have good sensitivity at high frequencies. This paper presents an algorithm by which a network can be “tuned”, in accordance with the best available information, in order to most effectively measure merger waves. The algorithm is presented in the context of a toy model that captures the qualitative features of narrow-band detectors and of certain binary neutron star merger wave models. By using what is learned from a sequence of merger measurements, the network can be gradually tuned in order to accurately measure the waves. The number of measurements needed to reach this stage depends upon the waves’ signal strength, the number of narrow-band detectors available for the measurement, and the detailed characteristics of the waves that carry the merger information. Future studies will go beyond this toy model, encompassing a more realistic description of both the detectors and the gravitational waves.

PACS numbers: 04.80.Nn, 95.55.Ym

I. INTRODUCTION

Much of the promise of gravitational-wave (GW) observation is in its potential as a novel probe of physics and astrophysics. Because GWs couple very weakly to matter and arise solely from gravitational interactions, sources that are completely dark electromagnetically may be strong GW emitters. By tracking and measuring the waves generated in violent astrophysical events, we may gain insight into physical processes that cannot be easily measured in other ways.

One example of such hard-to-measure physics is the late merger of compact binary systems. GW emission carries energy and angular momentum out of the binary, driving the compact bodies ever closer together. During the early *inspiral* portion of this coalescence process, the structure of the binary’s members plays little role; they can be usefully approximated as point masses, or spinning point masses. As the bodies come closer together, their internal structure becomes very important. The GWs generated in the final stages of *inspiral* and *merger*, when the bodies collide and merge into some coalesced state, will carry information about the bodies’ structure.

It has long been recognized that, if the binary contains at least one neutron star, merger waves will depend on the nature of neutron star matter (cf. Refs. [1, 2, 3, 4] and references therein). This opens the exciting possibility that GW measurements by detectors such as LIGO [5] could study the properties of very dense matter, such as its equation of state (EOS) [3, 6, 7]. Of particular interest will be testing whether neutron stars contain a core of “exotic” matter, such as a free quark state of some kind. Models of compact stars comprised of a free quark fluid, or with a free quark core, can have a structure rather different from ordinary neutron stars — they are often of smaller radius, and there may exist a sharp density transition at some finite radius from the star’s core [8, 9]. If one or both members of a binary system had such a structure, there could be an observable imprint on the merger GW signature. (We should emphasize, though, that much work remains to evaluate whether such a signature exists, and if so, what is its nature.)

Simulations of binary neutron star merger using Newtonian gravity and a polytropic EOS (see, e.g., [10, 11]) have found that the merger waves indeed carry information about the EOS, but that these waves are at very high frequency ($f \sim 1500 - 3000$ Hz) where broad-band LIGO-type detectors do not have good sensitivity. More recent work using irrotational matter configurations in the conformal approximation to GR [12] shows that the EOS-dependent structure is likely to come out at somewhat lower frequencies, $f \sim 1000$ Hz; this is still high enough that broad-band detector sensitivity is not very good. If one member of the binary is a black hole, the EOS-dependent information will come out at still lower frequencies, $f \sim 400 - 1000$ Hz [4] — the larger system mass shifts all frequencies downward. In this case, broad-band detectors are more useful for studying the merger waves, but still may not be ideal.

*Electronic address: hughes@kitp.ucsb.edu

To learn as much as possible from the waves generated during the merger, broad-band GW detectors should be supplemented by *narrow-band* detectors. Acoustic detectors in existence today [13, 14] and special interferometer topologies under development such as signal recycling [15] and resonant sideband extraction [16] have good sensitivity in a narrow band at high frequencies, $\delta f/f \sim 0.1-0.2$ for $f \sim 500-2500$ Hz. Narrow-band detectors answer essentially a yes-no question: “Did the binary radiate in my frequency band?” A “xylophone” of narrow-banded detectors would probe gross features of the merger waveform, such as a sharp cutoff in the GW spectrum (seen in recent simulations [12]), or the waves generated by a transient bar that forms in the merger detritus (seen in some Newtonian simulations [10, 11]). Such simple measurements should be robust in the sense that they wouldn’t require detailed modeling of the waves’ phasing — very important, since theoretical uncertainties in the merger waveforms are likely to be significant even when these measurements can be made.

Practical considerations such as cost and available facility space will limit the number of narrow-band detectors that can be used for each measurement. To make best use of these detectors, the network should be designed in a way that is in some sense optimal: the narrow-band detectors should be configured, in concert with the broad-band detectors, so that the network of all detectors is most likely to provide new information about merger waves, given our best present knowledge of the waves’ properties. How one “tunes” a detector network in this manner is the subject of this paper.

We assume that an inspiral has already been measured, so that we know merger waves must be present in the data. For the purposes of this analysis, we assume further that the waveform depends on a single parameter λ that grossly characterizes the merger waves. This λ could be the frequency of a sharp cutoff in the wave spectrum, or the frequency at which a short-lived bar may radiate for several cycles. Theoretical modeling allows us to phenomenologically relate this parameter to a description of the binary’s stars. For example, in models in which the wave spectrum sharply cuts off, λ is most strongly related to the compactness of the stars: smaller stars exhibit a cutoff at higher frequencies [12] since they spiral in further before the spectrum cuts off. Describing the merger features with a single parameter is no doubt an oversimplification, but is useful for demonstrating how network tuning works to zoom-in on gross features of the waves. Tuning the network means finding the configuration which measures λ with as little error as possible.

We develop a tuning algorithm that does just this: it configures the network to measure λ as accurately as possible, given our uncertainty in λ ’s value, and updates (“retunes”) the network as measurements teach us about merger waves. This algorithm is based on the maximum likelihood GW measurement formalism developed by Finn [17]. Finn defines two probability distributions which play a major role here: the *prior* probability, $p_0(\lambda)$, summarizing all that is known about λ before measurement; and the *posterior* probability, $P_{\text{post}}(\lambda|\hat{\lambda})$, summarizing what is known afterward. The posterior distribution is built from the measured datastream, and so explicitly depends upon the detector network’s characteristics and on the measured waveform $h(\hat{\lambda})$, where $\hat{\lambda}$ is the unknown, true value of λ .

Following measurement, the posterior probability is the tool one uses to estimate the values of the parameters describing GWs, and also to estimate the error in those values [17, 18, 19]. It is not quite the tool needed here: we need to estimate the accuracy with which λ is likely to be measured, but we need this estimate *before* measurement. To this end, we introduce an additional probability, the *anticipated* distribution of λ . This is a marginal distribution found by integrating out the dependence of the posterior probability upon the unknown true parameterization $\hat{\lambda}$:

$$P_{\text{ant}}(\lambda) = \int p_0(\hat{\lambda})P_{\text{post}}(\lambda|\hat{\lambda})d\hat{\lambda}. \quad (1.1)$$

This is the distribution that we we anticipate will describe λ after a measurement. Like the posterior probability, it depends on the detector network, so we can tune the network’s adjustable parameters to find the network which we anticipate will measure λ as accurately as possible, given our current ignorance of the merger waves.

From the anticipated distribution’s definition, it is simple to update and improve the network as we learn more about λ . Following a measurement, we construct the posterior distribution $P_{\text{post}}(\lambda|\hat{\lambda})$ from the datastream. We then use this posterior distribution as the prior distribution for the next measurement: $p_0^i(\lambda) = P_{\text{post}}^{i-1}(\lambda|\hat{\lambda})$. We update the anticipated distribution with the new priors, and then update the network. The detector network is thereby adjusted and improved following each measurement, so that our ability to measure λ is incrementally improved by each measurement. Our gradually improving knowledge of λ ’s value is manifested as a gradual peaking of this distribution: we begin with a prior describing complete ignorance (uniform distribution) and find that after several merger measurements the distribution begins to peak around the true value $\hat{\lambda}$. The more we learn about the merger waves, the more sharply peaked becomes this distribution.

In this paper, we demonstrate the concept and principles of network tuning using a toy model for the merger and for the narrow-band detectors. In Sec. II, we describe in more detail the probability distributions introduced above, and then discuss how we use them to tune our network designs. Our tuning procedure is given explicitly at the end of this section. We next present our toy model in Sec. III: we approximate narrow-band detectors as zero bandwidth (delta function) GW detectors with adjustable center frequency, and treat the waveform $h(t; \lambda)$ as a quadrupole inspiral

chirp up to a merger frequency $f_m \equiv \lambda \times 1000$ Hz. This highly simplified description throws away important physics, particularly the finite bandwidth expected in real narrow-band detectors and the slower frequency rolloff seen in recent merger computations (e.g., Ref. [12]). It is simple enough, though, that many of the calculations needed can be done analytically, and is close enough to the real problem that it should give a good sense of how network tuning is likely to proceed in practice.

We test our tuning algorithm in Sec. IV. We show that measurements can converge on an accurate value for λ after measuring some number of binary merger events. The size of that number depends on the signal strength (a few strong signals can drive convergence rather quickly) and the number of narrow-band detectors available for the measurement (having at least two available can speed up convergence quite a bit). The good behavior of our tuning procedure can be taken as an indication that this algorithm is robust. However, we cannot pretend that our analysis is in any way definitive: the toy description of the detectors and the waveform neglects several important effects. This analysis should therefore be regarded as a proof-of-concept presentation; future work, discussed in Sec. V, will put the various complications neglected here back where they belong. In particular, we plan to use more realistic descriptions of the narrow-band detectors (cf. Refs. [20, 21]), and merger waveforms taken from recent computational models.

II. FORMALISM

A. Probability distributions

As mentioned above, we assume that we have already detected a GW via the inspiral, and so we have already learned many interesting parameters characterizing the binary — combinations of the masses and spins, the distance to the binary to some accuracy, etc. [19, 22]. We now wish to measure the merger parameter λ .

Consider a network of N GW detectors. We use the notation of Appendix A of Ref. [23]: the datastream of the j -th detector in the network is g_j ; the output of the whole network is \vec{g} . Because we assume that a GW has been detected, this datastream consists of a GW signal $\vec{h}(\hat{\lambda})$ plus noise \vec{n} : $\vec{g} = \vec{h}(\hat{\lambda}) + \vec{n}$. (Recall that $\hat{\lambda}$ represents the true, unknown value of λ that describes the waves in the datastream.) Our goal is to determine the probability that, given this datastream, we will measure the parameter λ .

Our first step is to find the posterior probability that we measure the waveform $\vec{h}(\lambda)$ given the datastream \vec{g} . Finn has developed this probability for a single detector [17]; using the notation of Ref. [23], the generalization to multiple detectors is straightforward. Following Finn, we begin with Bayes' law:

$$P[\vec{h}(\lambda)|\vec{g}] = \frac{P[\vec{g}|\vec{h}(\lambda)]P[\vec{h}(\lambda)]}{P(\vec{g})}. \quad (2.1)$$

The probabilities written here have the same meaning as those used in Eq. (2.3) of [17]:

$$\begin{aligned} P[\vec{h}(\lambda)|\vec{g}] &= \text{the conditional probability that } \vec{h}(\lambda) \text{ is present given the datastream } \vec{g}; \\ P[\vec{g}|\vec{h}(\lambda)] &= \text{the conditional probability of measuring the datastream } \vec{g} \text{ given } \vec{h}(\lambda); \\ P[\vec{h}(\lambda)] &= \text{the prior probability that the waveform } \vec{h}(\lambda) \text{ is present} \\ &\equiv p_0(\lambda); \\ P(\vec{g}) &= \text{the probability that the datastream } \vec{g} \text{ is observed} \\ &\equiv 1. \end{aligned} \quad (2.2)$$

We have simplified the last two of these distributions. The first, $P[\vec{h}(\lambda)] \equiv p_0(\lambda)$, follows because by assumption the waveform depends only on λ . This is no doubt an oversimplification — other parameters, such as the mass ratio of the binary and its spins, are likely to have an important influence as well. To keep this analysis simple, we will focus on a single parameter model for the merger; this is adequate for now, and perfectly formulated for the toy model presented in Sec. III. The second simplification, $P(\vec{g}) = 1$, follows because \vec{g} has already been measured and is therefore determined. Here we depart a bit from the analysis of Ref. [17] — Finn does *not* assume that this particular datastream \vec{g} has already been measured. His \vec{g} is *undetermined*, and has a non-trivial probability distribution.

The distribution $P[\vec{g}|\vec{h}(\lambda)]$ used here is identical to that used by Finn (modulo the extension to multiple detectors). It answers the question “What is the probability that, if the data contains the GW $\vec{h}(\lambda)$, noise is present such that $\vec{n} + \vec{h}(\lambda)$ is consistent with the observed data stream \vec{g} ?” This shows that $P[\vec{g}|\vec{h}(\lambda)]$ is equivalent to $P[\vec{g} - \vec{h}(\lambda)|0]$, the probability that $\vec{g} - \vec{h}(\lambda)$ is pure noise. Under the assumption that the noise is Gaussian, this is [17]

$$P[\vec{g}|\vec{h}(\lambda)] = \mathcal{K} \exp \left[-\frac{1}{2} \left(\vec{g} - \vec{h}(\lambda) | \vec{g} - \vec{h}(\lambda) \right) \right], \quad (2.3)$$

where the inner product is given by

$$\left(\vec{a}|\vec{b}\right) \equiv 4 \operatorname{Re} \int_0^\infty \tilde{a}_j(f)^* [\mathbf{S}_h(f)^{-1}]^{jk} \tilde{b}_k(f) df, \quad (2.4)$$

and \mathcal{K} is a normalization constant. Here, $\tilde{a}_j(f)$ is the Fourier transform of $a_j(t)$:

$$\tilde{a}_j(f) = \int_{-\infty}^\infty a_j(t) e^{2\pi i f t} dt, \quad (2.5)$$

and the asterisk denotes complex conjugation. The matrix $\mathbf{S}_h(f)$ is a generalization of the (one-sided) strain noise spectral density. Diagonal components $\mathbf{S}_h(f)_{jj}$ represent the usual spectral density for detector j ; off-diagonal elements represent correlations between detectors j and k . For more details, see Appendix A of Ref. [23]. Combining these distributions, using $\vec{g} = \vec{h}(\hat{\lambda}) + \vec{n}$, and defining $\delta\vec{h} \equiv \vec{h}(\hat{\lambda}) - \vec{h}(\lambda)$ yields

$$P[\vec{h}(\lambda)|\vec{g}] = \mathcal{K} p_0(\lambda) \exp\left[-\frac{1}{2}(\delta\vec{h}|\delta\vec{h}) - (\vec{n}|\delta\vec{h}) - \frac{1}{2}(\vec{n}|\vec{n})\right]. \quad (2.6)$$

Equation (2.6) depends on the specific noise instance $\vec{n}(t)$ present in the detector network. We circumvent this by taking a ‘‘frequentist’’ viewpoint and ensemble averaging Eq. (2.6) with respect to the noise. The resulting distribution is our posterior distribution for λ , given data containing $\hat{\lambda}$:

$$\begin{aligned} P_{\text{post}}(\lambda|\hat{\lambda}) &\equiv p_0(\lambda) \mathbb{E}_{\vec{n}} \left\{ P[\vec{h}(\lambda)|\vec{g}] \right\} \\ &= p_0(\lambda) \int P(\vec{n}) P[\vec{h}(\lambda)|\vec{g}] \mathcal{D}\vec{n} \\ &= \mathcal{K} p_0(\lambda) \int \mathcal{D}\vec{n} \exp\left[-\frac{1}{2}(\vec{n}|\vec{n})\right] \exp\left[-\frac{1}{2}(\delta\vec{h}|\delta\vec{h}) - (\vec{n}|\delta\vec{h}) - \frac{1}{2}(\vec{n}|\vec{n})\right]. \end{aligned} \quad (2.7)$$

The final integral is a functional integral, taken over all possible network noise instances \vec{n} . We evaluate it in Appendix A; the result is

$$P_{\text{post}}(\lambda|\hat{\lambda}) = \mathcal{K} p_0(\lambda) \exp\left[-\frac{1}{4}(\delta\vec{h}|\delta\vec{h})\right]. \quad (2.8)$$

This distribution is normalized so that $\int P_{\text{post}}(\lambda|\hat{\lambda}) d\lambda = 1$. The normalization constant \mathcal{K} thus depends on $\hat{\lambda}$ and the noise characteristics.

As discussed in the Introduction, $P_{\text{post}}(\lambda|\hat{\lambda})$ is not useful for designing a detector network since it is constructed after measurement. This is reflected by its implicit dependence on $\hat{\lambda}$. A more useful quantity is obtained by marginalizing on $\hat{\lambda}$. This gives a distribution which represents the posterior distribution that we *anticipate* will describe the λ after measurement, modulo our ignorance about $\hat{\lambda}$:

$$P_{\text{ant}}(\lambda) = \int p_0(\hat{\lambda}) P_{\text{post}}(\lambda|\hat{\lambda}) d\hat{\lambda}. \quad (2.9)$$

The anticipated distribution answers the question ‘‘How is λ likely to be distributed given our ignorance about the neutron star merger waveform?’’

B. Tuning the detector network

We now choose the detector configuration that we anticipate will measure λ as accurately as possible. Consider the mean and variance of the distribution (2.9):

$$\bar{\lambda}_{\text{ant}} = \int \lambda P_{\text{ant}}(\lambda) d\lambda, \quad (2.10)$$

$$\begin{aligned} \sigma_{\text{ant}}^2 &= \int (\lambda - \bar{\lambda}_{\text{ant}})^2 P_{\text{ant}}(\lambda) d\lambda, \\ &= \int \lambda^2 P_{\text{ant}}(\lambda) d\lambda - \bar{\lambda}_{\text{ant}}^2. \end{aligned} \quad (2.11)$$

The mean is indicative of the typical value of λ that a particular observation will measure. Likewise, the variance (2.11) is an indicator of how accurately λ will be measured; we anticipate that a measurement will typically find λ within σ_{ant} of $\bar{\lambda}_{\text{ant}}$.

Through the inner product (2.4), the variance (2.11) depends on the characteristics of the detector network. Some of these characteristics will depend on adjustable parameters, such as the central frequencies of narrow-band detectors. Let the k th such adjustable parameter be μ_k . The network which minimizes σ_{ant} is the one which we anticipate will measure λ most accurately:

$$\min_{\mu_k} \sigma_{\text{ant}}^2 \mapsto \text{The optimally tuned network} . \quad (2.12)$$

We call the process of finding the parameters which minimize σ_{ant}^2 “tuning”; the network so produced is “optimally tuned” or simply “optimal”.

Because of the non-Gaussian nature of the relevant distributions, a variance such as σ_{ant}^2 is a less than ideal measure of error. If we were truly interested in characterizing the error of a measurement, we would instead study contours of a likelihood function (see, e.g., Refs. [17, 18]). However, σ_{ant}^2 is very easy to compute, and has the correct qualitative behavior — it will get smaller as more rigorous measures of error decrease. Tuning our network in such a way that σ_{ant}^2 is minimized will drive more rigorous notions of error to be small as well.

Since $P_{\text{post}}(\lambda|\hat{\lambda})$ is built from the measured data, it depends on the measurement’s signal-to-noise ratio (SNR). Thus the anticipated probability, and the optimal network it produces, likewise depend on SNR. This is arguably a weakness of this prescription for network tuning — the network found by minimizing σ_{ant}^2 depends explicitly upon the anticipated strength of the waves that we hope to measure. For our present purposes, we believe that leaving the SNR in the algorithm as an adjustable parameter is actually desirable. Properly eliminating the SNR dependence would require integrating it out with a correctly constructed probability function for its distribution. Although there exist estimates of the compact binary coalescence rate which we could use to construct such a function, these estimates are currently rather uncertain [24, 25]. By the time that the interferometer configurations we consider here can be installed, LIGO-type detectors could be detecting many events per year, or just a few. If many are detected, then observers may choose to focus their merger analyses on the strongest events in this large set. On the other hand, if the rate turns out to be low, observers will be forced to work with relatively weak signals. It is therefore useful to see how SNR choice affects network design, exploring how tuning will work as a function of the SNR levels that turn out to be appropriate. Accordingly, we choose to leave in the SNR as a parameter for now.

Finally, note that the prior probability $p_0(\lambda)$ plays a crucial role, through Eqs. (2.8) and (2.9), in determining the optimal detector network. This gives a natural way to update the network as our knowledge of merger waves improves: we continually update the priors as we learn more about λ , and concomitantly update the network to zoom-in on the true value of λ . This updating is the key element of the network tuning algorithm.

Explicitly, this algorithm works as follows:

1. Before the first merger is measured, our understanding of λ is likely to be crude. Take the prior distribution to be uniform between some upper and lower limits: $p_0(\lambda) = \text{const}$, $\lambda_{\text{MIN}} \leq \lambda \leq \lambda_{\text{MAX}}$.
2. Configure the detector network by minimizing Eq. (2.11) with this uniform prior.
3. Measure a merger. Build the posterior distribution $P_{\text{post}}(\lambda|\hat{\lambda})$ [Eq. (2.8)] from the measured data.
4. Use this posterior distribution as the prior for the next measurement: set $p_0^{\text{new}}(\lambda) = P_{\text{post}}(\lambda|\hat{\lambda})$.
5. Reconfigure the network by minimizing (2.11) with this prior.
6. Go to 3.

As we will show in Sec. IV, this algorithm effectively zooms in on the true parameterization $\hat{\lambda}$ of the waves in the datastream, at least for the toy model we present next.

III. TOY MODEL

Here we describe the simplified model we use for the waveform (Sec. III A) and for the detector noise (Sec. III B). These models make it possible to evaluate the posterior distribution analytically (Sec. III C). We discuss the shortcomings of this toy description in Sec. III D. We plan to address these shortcomings in future work.

A. Waveform

The gravitational waveform has two polarizations, h_+ and h_\times (named for the axes of force lines associated with them). Each detector in the network measures some linear combination of these polarizations:

$$h_j = F_{j,+}h_+ + F_{j,\times}h_\times. \quad (3.1)$$

The functions $F_{j,+,\times}$ depend on the type of GW detector used for the measurement. For interferometers, standard formulae for $F_{+,\times}$ are given in, e.g., Ref. [2] [Eqs. (104a,b) and preceding text]. For certain spherical acoustic detectors (cf. Ref. [13] and references therein), $F_+ \simeq F_\times \simeq \text{const}$ — spherical antennae have nearly equal sensitivity to both polarizations, independent of the source's sky position.

The polarizations of the leading quadrupole harmonic of the inspiral waveform are, in the frequency domain,

$$\begin{aligned} \tilde{h}_+(f) &= 2(1 + \cos^2 \iota) \tilde{h}_Q(f), \\ \tilde{h}_\times(f) &= 4 \cos \iota e^{i\pi/2} \tilde{h}_Q(f); \\ \tilde{h}_Q(f) &\equiv \sqrt{\frac{5}{96}} \frac{\pi^{-2/3} \mathcal{M}^{5/6}}{r} f^{-7/6} e^{i\Phi(f)}. \end{aligned} \quad (3.2)$$

The angle ι is between the line of sight to the binary and its orbital angular momentum, r is the distance to the source, $\mathcal{M} \equiv (m_1 m_2)^{3/5} / (m_1 + m_2)^{1/5}$ is the binary's "chirp mass", and $\Phi(f)$ is a phase function, described further below.

To make our toy model for the waveform, we first simplify this inspiral in two ways. First, we restrict ourselves to equal mass binaries: we set $m_1 = m_2 = 1.4 M_\odot$. Since we are focusing on neutron star binaries, this is not a drastic simplification. Second, we use only the Newtonian, quadrupole contribution to the phase, ignoring higher-order post-Newtonian contributions:

$$\Phi(f) = 2\pi f t_c - \phi_c - \frac{\pi}{4} + \frac{3}{4} (8\pi \mathcal{M} f)^{-5/3}, \quad (3.3)$$

where t_c is the time at which the frequency (formally) diverges to infinity, and ϕ_c is the phase at that time.

To represent the transition from inspiral to merger, we multiply $h_{+,\times}$ by $\Theta(\lambda f_{\text{kHz}} - f)$, where Θ is the step function and $f_{\text{kHz}} = 1000$ Hz. We assume that λ lies between 0.5 and 1.5; this is consistent with the results seen in Ref. [12]. This extremely simple waveform captures the essence of coalescence models in which the GWs shut off very rapidly as the neutron stars come into contact with one another. Because we neglect higher order contributions to the phasing, and because our model shuts off the wave emission far more rapidly than is seen in any actual calculation, our results should be considered illustrative rather than definitive.

The frequency domain GW signal measured in detector j of the network is therefore

$$\tilde{h}_j(f) = \left[2(1 + \cos^2 \iota) F_{j,+} + 4 \cos \iota e^{i\pi/2} F_{j,\times} \right] \tilde{h}_Q(f) \Theta(\lambda f_{\text{kHz}} - f). \quad (3.4)$$

A very useful quantity which we can calculate from this waveform is the SNR ρ_j :

$$\begin{aligned} \rho_j^2 &= 4 \int_0^\infty \frac{|\tilde{h}_j(f)|^2}{S_h(f)_j} df \\ &= \frac{5 |\Psi_j|^2 \pi^{-4/3} \mathcal{M}^{5/3}}{24 r^2} \int_0^{\lambda f_{\text{kHz}}} \frac{f^{-7/3}}{S_h(f)_j} df. \end{aligned} \quad (3.5)$$

The first line is a standard formula for the SNR of a GW measurement (cf. Refs. [17, 18, 19]). The quantity $S_h(f)_j$ is the spectral density of noise in the j -th detector; we discuss our toy description of this quantity in the following section. In the second line, we have specialized to the toy waveform. We have introduced here the angular function

$$|\Psi_j|^2 = 4 \left[(1 + \cos^2 \iota)^2 F_{j,+}^2 + 4 \cos^2 \iota F_{j,\times}^2 \right]. \quad (3.7)$$

Note that $|\Psi_j|^2$ is identical to the Θ^2 defined in Ref. [18]; we use a slightly different notation to avoid confusion with the step function. This function lies in the range $0 \leq |\Psi_j|^2 \leq 16$; its value averaged over all sky positions and source orientation angles is $\overline{|\Psi_j|^2} = 2.56$. The distribution of $|\Psi_j|^2$ is quite asymmetric, with values smaller than $\overline{|\Psi_j|^2}$ more likely than larger ones. See Ref. [18] for further discussion.

We plot a representation of this waveform in Fig. 1, comparing it to our model of the detector noise (discussed in detail in the following section). The waveform plotted here is somewhat massaged — we actually plot

$$h_{\text{plot}}(f) = \sqrt{f|\tilde{h}(f)|^2}. \quad (3.8)$$

This quantity has the same units as the noise spectrum, and has the nice feature that the integral of $h_{\text{plot}}(f)^2$ over the noise is the squared signal-to-noise ratio ρ^2 : using Eq. (3.5), we see that

$$\rho_j^2 = 4 \int d \ln f \frac{h_{\text{plot}}(f)_j^2}{S_h(f)_j}. \quad (3.9)$$

The waveform we show corresponds to a pair of $1.4 M_\odot$ neutron stars with optimal orientation ($|\Psi|^2 = 16$) at 500 Mpc; or, with “average orientation” ($|\Psi|^2 = 2.56$) at 200 Mpc. We have chosen $\lambda = 0.8$, so that the waveform’s merger cutoff is at 800 Hz.

Inserting the toy waveform (3.4) into Eq. (2.8) yields

$$\begin{aligned} P_{\text{post}}(\lambda|\hat{\lambda}) = & p_0(\lambda) \exp \left[-\text{Re} \int_0^\infty [2(1 + \cos \iota^2) F_{j,+} + 4 \cos \iota e^{i\pi/2} F_{j,\times}] [2(1 + \cos \iota^2) F_{k,+} \right. \\ & \left. + 4 \cos \iota e^{i\pi/2} F_{k,\times}] \left[\Theta(\hat{\lambda} f_{\text{kHz}} - f) - \Theta(\lambda f_{\text{kHz}} - f) \right]^2 |\tilde{h}_Q(f)|^2 [\mathbf{S}_h(f)^{-1}]^{jk} df \right]. \end{aligned} \quad (3.10)$$

Define $\lambda_{\text{LO}} \equiv \min(\hat{\lambda}, \lambda)$, $\lambda_{\text{HI}} \equiv \max(\hat{\lambda}, \lambda)$. Because of the Θ functions in Eq. (3.10), the domain of integration is restricted to the range $f_{\text{LO}} \leq f \leq f_{\text{HI}}$ (where $f_{\text{LO}} = \lambda_{\text{LO}} f_{\text{kHz}}$, $f_{\text{HI}} = \lambda_{\text{HI}} f_{\text{kHz}}$). For the range of λ that we have selected, the detector noise in the merger band is dominated by laser shot noise. We will use this to simplify Eq. (3.10) further in what follows.

B. Detector noise

Very detailed parameterized models for the LIGO noise budget exist and can be manipulated using codes such as BENCH [26] (which was used for the analysis of [21]). For our purposes, much simpler descriptions that are simple to manipulate analytically will be mostly adequate.

We will take our broad-band detectors to have the noise curve anticipated for the second-generation LIGO detectors (“LIGO-II noise”), as described in Refs. [20, 21]. In particular, since we focus on measurements of binary neutron star inspiral, we will assume the broad-band measurements are made using the interferometer configuration optimized for that source (the curve labeled “NS-NS” in Figure 1 of Ref. [20]); we show it in Fig. 1.

The NS-NS LIGO-II noise profile we use is a broad-band signal-recycled configuration. In the shot noise dominated band, its noise spectrum grows with an f^2 law:

$$\begin{aligned} S_h^{\text{BB}}(f) &= \gamma_{\text{NS-NS}} f^2 \\ &= (1.5 \times 10^{-52} \text{ Hz}^{-3}) f^2. \end{aligned} \quad (3.11)$$

The numerical value of the parameter $\gamma_{\text{NS-NS}}$ given here was found by fitting to the high-frequency end of the NS-NS LIGO-II noise curve given in [20].

We will take our narrow-band detectors to be LIGO-II detectors operated in a narrow-band configuration; cf. discussion in Refs. [20, 21]. A detailed description of the noise in this configuration can be found using BENCH; near the most sensitive frequency of such a configuration, it is well described by the approximate formula [2, 27, 28]

$$S_h^{\text{NB}}(f) \simeq 2S_0 \left(\frac{\Delta f}{f_0} \right) \left[1 + 4 \left(\frac{f - f_R}{\Delta f} \right)^2 \right]. \quad (3.12)$$

The parameters S_0 and f_0 appearing here are

$$S_0 = \frac{\hbar \lambda_L c}{4\pi \eta I_0} \left(\frac{\beta}{L} \right)^2 \simeq 2.1 \times 10^{-51} \text{ Hz}^{-1}, \quad (3.13)$$

$$f_0 = \frac{\beta c}{4\pi L} \simeq 0.2 \text{ Hz}. \quad (3.14)$$

The numerical values of the laser wavelength λ_L , laser power I_0 , photodiode efficiency η , mirror power loss β , and armlength L are given in Table II of Ref. [21]. The frequency f_R is controlled by the position of one of the mirrors in the narrow-banded interferometer, and as such is not too difficult to adjust; it might even be possible to *dynamically* adjust this position, in order to track the evolution of a particularly interesting feature.

The bandwidth Δf is rather more complicated. It is largely set by losses in the mirrors, but also depends in an important way on the position of the mirror that controls f_R . Hence, as we tune f_R , the bandwidth changes as well. For the purpose of our toy model, we will ignore this effect; examples of the toy narrow-band noise spectrum (with fixed bandwidth) are shown in Fig. 1. We emphasize that the bandwidth *cannot* be treated as constant in a realistic analysis. Indeed, there are many coupled effects that appear when a realistic description of a narrow-band interferometer is used. For example, configurations that improve detector response in a narrow-band at high frequency can actually improve response at low frequency as well [29, 30].

For the toy model, we will approximate the narrow-band detectors as having infinitesimal bandwidth:

$$\frac{1}{S_h^{\text{NB}}(f)} \simeq \frac{\pi f_0}{4S_0} \delta(f - f_R). \quad (3.15)$$

This form is particularly easy to use, and is not a bad description of the interferometer response around the center frequency when the bandwidth is very narrow. The prefactor is chosen so that the integral of $1/S_h^{\text{NB}}(f)$ is the same for Eqs. (3.12) and (3.15). We will treat the frequency f_R of each narrow-band detector in our network as an adjustable parameter, and tune our network by varying those frequencies to find the optimal network for measuring merger waves. Note that by using such a narrow detector response, we throw away potentially useful information. This is an obvious point of improvement for an analysis that goes beyond this toy model.

C. Evaluation of the posterior probability

We now use the toy description of the noise to evaluate analytically the posterior probability distribution (3.10). First, we assume that the various individual detectors on the network have uncorrelated noises: we set the off-diagonal terms in the matrix $\mathbf{S}_h(f)^{-1}$ to zero. This should be a reasonable assumption in the high frequency, shot-noise-dominated regime appropriate to this analysis — each interferometer will have its own laser and optics system, and should therefore be reasonably isolated from all other detectors (though events affecting interferometers at a common site could violate this assumption). Equation (3.10) then simplifies to

$$P_{\text{post}}(\lambda|\hat{\lambda}) = p_0(\lambda) \exp \left[- \sum_{j=1}^N |\Psi|_j^2 \int_{f_{\text{LO}}}^{f_{\text{HI}}} \frac{|\tilde{h}_Q(f)|^2}{S_h(f)_j} df \right], \quad (3.16)$$

where N is the total number of detectors, broad-band plus narrow-band.

To simplify this analysis further, we will assume that all detectors are housed within a single facility, so that the functions $|\Psi|_j^2$ take a single value $|\Psi|^2$ for all j . Further, we will assume there is only one broad-band detector in this facility, and N_N narrow-band detectors. The sum in the exponent of Eq. (3.16) can now be simplified:

$$\sum_{j=1}^N |\Psi|_j^2 \int_{f_{\text{LO}}}^{f_{\text{HI}}} \frac{|\tilde{h}_Q(f)|^2}{S_h(f)_j} df = |\Psi|^2 \int_{f_{\text{LO}}}^{f_{\text{HI}}} \frac{|\tilde{h}_Q(f)|^2}{S_h^{\text{BB}}(f)} df + |\Psi|^2 \sum_{j=1}^{N_N} \int_{f_{\text{LO}}}^{f_{\text{HI}}} \frac{|\tilde{h}_Q(f)|^2}{S_h^{\text{NB}}(f)_j} df. \quad (3.17)$$

Using Eqs. (3.11) and (3.15), these integrals are simple to evaluate. The result is

$$P_{\text{post}}(\lambda|\hat{\lambda}) = p_0(\lambda) \exp \left[- \frac{3}{20} \frac{\rho_{\text{insp}}^2}{\sigma_7} \frac{1}{\gamma_{\text{NS-NS}}} f_{\text{kHz}}^{-10/3} \left| \frac{1}{\hat{\lambda}^{10/3}} - \frac{1}{\lambda^{10/3}} \right| - \frac{\pi}{16} \frac{\rho_{\text{insp}}^2}{\sigma_7} \frac{f_0}{S_0} f_{\text{kHz}}^{-7/3} \sum_{j=1}^{N_N} \left(\frac{f_{\text{kHz}}}{f_{R,j}} \right)^{7/3} \left| \Theta(\hat{\lambda} f_{\text{kHz}} - f_{R,j}) - \Theta(\lambda f_{\text{kHz}} - f_{R,j}) \right| \right]. \quad (3.18)$$

The frequency $f_{R,j}$ is the adjustable frequency of peak sensitivity for the j -th narrow-band detector. The step functions enforce the fact that the integral over the narrow-band noise is non-zero only if $f_{\text{LO}} < f_{R,j} < f_{\text{HI}}$. We have simplified this expression considerably by normalizing the amplitude of the GWs to the inspiral SNR ρ_{insp} measured

in the broad-band detector. Using Eq. (3.6),

$$\begin{aligned}\rho_{\text{insp}}^2 &\simeq \frac{5|\Psi|^2 \pi^{-4/3} \mathcal{M}^{5/3}}{24 r^2} \int_0^\infty \frac{f^{-7/3}}{S_h^{\text{BB}}(f)} df \\ &= \frac{5|\Psi|^2 \pi^{-4/3} \mathcal{M}^{5/3}}{24 r^2} \sigma_\tau.\end{aligned}\quad (3.19)$$

Taking the upper limit of the integral to infinity (rather than $\lambda \times 1000$ Hz) is fine for the inspiral SNR since most of the signal accumulates near $f \sim 100$ Hz — the upper frequency has little effect. With the broad-band LIGO-II noise curve used here, $\sigma_\tau = 8.3 \times 10^{44} \text{ Hz}^{-1/3}$. For a binary consisting of a pair of $1.4 M_\odot$ neutron stars, the SNR becomes

$$\rho_{\text{insp}} = 11.7 \left(\frac{|\Psi|^2}{2.56} \right)^{1/2} \left(\frac{200 \text{ Mpc}}{r} \right).\quad (3.20)$$

With this parameterization, we see how the tuning algorithm will depend upon SNR, as described in Sec. II B. Note that, in this toy model, the inspiral SNR and the frequency $f_{R,j}$ completely determine the SNR measured in the j -th narrow-band detector:

$$\begin{aligned}\rho_{\text{NB},j}^2 &= 4 \int_0^\infty \frac{|\tilde{h}_Q(f)|^2}{S_h^{\text{NB}}(f)_j} df \\ &= \frac{\pi}{16} \frac{\rho_{\text{insp}}^2 f_0}{\sigma_\tau S_0} f_{R,j}^{-7/3}.\end{aligned}\quad (3.21)$$

Plugging in the values of f_0 , S_0 , and σ_τ , we find

$$\frac{\rho_{\text{NB}}}{\rho_{\text{insp}}} = 0.05 \left(\frac{1000}{f_{R,j}} \right)^{7/6}.\quad (3.22)$$

The narrow-band SNR drops off very quickly with frequency. This follows directly from our toy model for the waveform — the amplitude decays with frequency as $f^{-7/6}$ up to the step function break, so the SNR decays likewise.

The anticipated probability distribution is found by plugging (3.18) into (2.9). It is best evaluated numerically.

D. Shortcomings of this toy description

Although useful for demonstrating how network tuning works, we cannot pretend that the toy model is anything more than illustrative. First, the waveform we use [Eq. (3.2)] is drastically oversimplified. Although it produces an energy spectrum qualitatively similar to that seen in recent computations (e.g., Ref. [12]), it shuts off the inspiral waves far more quickly than those calculations predict. In the spectra developed in Ref. [12], the GW energy emission drops from the (relatively large) level of the quadrupole inspiral by about an order of magnitude over a band of a few hundred Hz. By not rolling off more gradually, the toy waves are likely too large as the merger frequency λf_{kHz} is approached. Second, the infinitesimal bandwidth (3.15) we use for the narrow-band detectors does not describe the configurations that will be used in realistic second generation interferometers — the actual detectors will have some finite bandwidth of tens to hundreds of Hz.

The toy model captures enough of the “feel” of the real problem that we are confident this analysis should be a useful demonstration of how network tuning will work with realistic waves and detectors. Nonetheless, because of the details that have been thrown away, we emphasize that this analysis must be followed up by calculations that are not oversimplified. The interplay between these neglected features is likely to be rather important — for instance, the finite bandwidth of the real narrow-band detectors may help to detect the relatively slow shut off that may describe merger waves in nature. This would also be an opportunity to test out ideas such as dynamical tuning of narrow-band detectors.

IV. RESULTS

We now test the network tuning algorithm on the toy model. We implement tuning by numerically finding the minima of the anticipated variance σ_{ant}^2 [which is itself built from a numerical construction of the anticipated distribution, using Eq. (3.18) in Eq. (2.9)]. This was done with Powell’s multidimensional line minimization technique,

using Brent’s method for the successive line minimizations (cf. Ref. [31]). This approach works very well at finding local minima. If the number of minima is not too large, one can simply compute the set of all local minima, then find the global minimum of σ_{ant}^2 in that set. This is adequate for the toy model provided that the number of narrow-band detectors is not too large. It may not work nearly so well when more realistic waveforms and noise models are used; robust global minimization methods (e.g., simulated annealing) might work better in this case.

Before examining merger measurements in detail, we discuss at some length the detector networks that tuning produces (Sec. IV A). The toy model is simple enough that we can easily understand why this algorithm tunes the network to the parameters that it chooses; we expect that the intuition developed here should apply more generally. We then look at merger measurement in Sec. IV B. We begin with a uniform prior distribution for λ (imagining that, aside from an upper and a lower bound, we are completely ignorant of λ ’s value) and show that repeated measurements of NS-NS merger drive the distribution to gradually peak on the true value $\hat{\lambda}$. We look at this process at two SNR levels ($\rho_{\text{insp}} = 10$ and 30), and consider measurement using 1 and 2 narrow-band detectors.

A. Optimal detector networks

Since our network tuning procedure works by minimizing σ_{ant}^2 , it is useful to understand this quantity’s properties. Figure 2 shows the anticipated variance when measurements are made with a single narrow-band detector. We assume a uniform prior distribution for λ between $\lambda = 0.5$ and $\lambda = 1.5$, and show results for inspiral SNR $\rho_{\text{insp}} = 10$ (upper panel) and 90 (lower panel).

In both cases, we see two minima: one is in the vicinity of 600 – 800 Hz, the other is near 1200 – 1400 Hz. For $\rho_{\text{insp}} = 10$, the lower frequency minimum is the global minimum; for $\rho_{\text{insp}} = 90$, the reverse holds. This interesting result has a simple explanation. As we move to higher frequencies, the broad-band detector’s shot noise grows increasingly more important, with a spectrum proportional to f^2 . This makes it advantageous to place a narrow-band detector at high frequency, where it can compensate for the broad-band detector’s degrading performance. However, our assumed waveform (3.4) gets very weak at high frequencies: the amplitude (prior to the cutoff enforced by the step function) decays with frequency as $f^{-7/6}$. The SNR measured by a high-frequency narrow-band detector is potentially very small [cf. Eq. (3.22)], and we are more likely to get a “false positive” — an incorrect signal measurement due to noise at high frequencies. These two phenomena compete. Which of these two dominates in the end depends upon the overall signal amplitude (here set by the inspiral SNR).

At low SNR, the need to avoid false positives tends to win out — the low frequency minimum at $f \sim 630$ Hz is the global minimum of σ_{ant}^2 . As the signal strength is increased, the danger of false positives decreases. At $\rho_{\text{insp}} = 90$, the tuning algorithm places the narrow-band detector at $f \sim 1380$ Hz — the signal is strong enough that the tuning algorithm chooses to compensate for the degraded sensitivity of the broad-band detector.

This pattern of minima location for uniform prior distribution — a high frequency minimum near $f \sim 1200 - 1400$ Hz, a low frequency minimum near $f \sim 600 - 800$ Hz — holds as we increase the number of narrow-band detectors. Table I shows the narrow-band detector frequencies that minimize σ_{ant}^2 for inspiral SNR 10, 30, and 90. Note that for $\rho_{\text{insp}} = 10$, the tuning algorithm *always* places the narrow-band detectors at low frequency, even for $N_N = 5$. At higher SNR, it tends to distribute the detectors more evenly.

It’s worth noting at this point that we assume the noise statistics of all our detectors is Gaussian, and hence our discussion of the likelihood of “false positives” is based on what may be a somewhat optimistic assumption of how the detectors will behave. (Since we assume that an inspiral signal has been detected and that the merger waves rapidly follow, Gaussianity may not be terribly optimistic — non-Gaussian events which violate this assumption will have to occur in a very narrow, specific time window.) Using multiple detectors in a similar band has the additional benefit of serving as checks on one another; it is difficult to know how one’s instruments will behave until they have been studied and their statistical behavior is known.

B. Measurement sequences

Next we examine measurement sequences, following the algorithm outlined at the end of Sec. II. As already mentioned, the key element of this algorithm is updating the priors after each measurement: we replace the prior distribution $p_0(\lambda)$ with the posterior distribution built from the measured data, $P(\lambda|\hat{\lambda})$. In this simulated sequence of measurements, we assume for simplicity that each measurement in the sequence has identical SNR; we also (as discussed in Sec. II) use a posterior distribution that has been ensemble averaged with respect to the noise. A more realistic calculation would randomly pick a noise realization from the distribution of possible noise functions, and would allow the SNR to vary from measurement to measurement in accordance with estimates of the distribution of binary inspiral events.

We first look at how well detector networks can measure λ for moderate inspiral SNR ($\rho_{\text{insp}} = 10$) and with a single narrow-band detector. We show a measurement sequence for $\hat{\lambda} = 0.8$ in Fig. 3. The upper left hand panel shows the posterior probability that would be obtained if no narrow-band detectors were used for the measurement. It is practically flat — there is essentially no information about λ in this distribution. The other panels show how the distribution evolves as multiple measurements are made using a narrow-band detector. The distribution gradually becomes peaked as more and more measurements are made. Network tuning “zooms-in” on the true merger parameterization $\hat{\lambda}$, placing the narrow-banded detector where it most effectively measures the merger waves. After 9 measurements, the distribution is clearly peaked around $\hat{\lambda}$; it is markedly peaked after 15 measurements. Such a strongly peaked distribution indicates that λ has been measured very accurately — the narrowness of the distribution means that the error in λ ’s determination is very small.

When $\hat{\lambda} = 1.2$, it takes many more measurements before the distributions become peaked; this is shown in Fig. 4. This is not surprising — the merger features are at 1200 Hz in this case, not 800 Hz, and so the expected narrow-band SNR is smaller by a factor of $(800/1200)^{7/6} = 0.6$. Because of the low SNR, the tuning algorithm tends to avoid placing the detector at high frequencies. The algorithm walks the narrow-band detector up to high frequency fairly slowly, doing so at a rate that ensures we have ruled out a low value of $\hat{\lambda}$ before “testing the waters” at high values. After 25 measurements, we have narrowed down to a relatively broad distribution centered at $\lambda \sim 1.1$; after a total of 50 measurements, the distribution is strongly peaked near $\hat{\lambda}$.

Figure 5 shows a sequence equivalent to that used for Fig. 4, but now using two narrow-band detectors. The convergence onto the true parameterization is quite a bit quicker in this case. With two narrow-band detectors, the tuning algorithm has much more freedom to choose how it zooms in on the merger waves than when only one is used — the detectors can be placed at both ends of the merger frequency space and slide inward, or both can be placed at one end. In the case shown, the distribution found after 28 measurements with two narrow-band detectors is nearly the same as it was after 50 measurements with one narrow-band detector.

The posterior distribution becomes peaked near $\hat{\lambda}$ much more quickly if the measurements include several events at higher SNR. Figure 6 shows the convergence of the distribution for $\hat{\lambda}$ when each measurement is at $\rho_{\text{insp}} = 30$ rather than 10. There is much less danger of a false positive at this SNR level, so the algorithm is able to zoom in on the true parameterization much more aggressively. As a consequence, the distribution is sharply peaked after only nine measurements — λ is measured quite accurately relatively quickly at this SNR. The convergence is even quicker when $\hat{\lambda} = 0.8$: although we do not show the corresponding plots, we find that the posterior distributions become quite peaked about $\hat{\lambda}$ after only 4 measurements with $\rho_{\text{insp}} = 30$.

V. CONCLUSIONS AND DIRECTIONS FOR FURTHER WORK

The results of the previous section show that network tuning works effectively, at least within the context of the toy model: in all cases, we find that after some number of measurements the probability distribution describing what is known about λ will become sharply peaked about $\hat{\lambda}$. The number of measurements that are needed depends quite a bit on the particulars of the waveform and of the detector network used. In particular, we can draw two conclusions that are not at all surprising:

- Multiple narrow-band detectors helps the measurement process greatly. In particular, the improvement in going from one narrow-band detector to two detectors can be significant.
- The rate at which measurements converge onto an accurate description of the merger waves depends strongly on those waves’ measured SNR. These can be seen in the drastic difference in the convergence of measurement sequences for $\hat{\lambda} = 0.8$ and $\hat{\lambda} = 1.2$ at fixed inspiral SNR (Fig. 3 versus Fig. 4) and in the drastic difference seen when the wave amplitude is increased by a factor of 3 (Fig. 4 versus Fig. 6).

From the first of these conclusions, we advocate investigating the possibility of running at least two detectors in the world-wide GW detector network in a narrow-band configuration. For example, LIGO already has 3 running interferometers (a 4 km broad-band detector and a 2 km broad-band detector at Hanford, Washington, plus a 4 km broad-band detector at Livingston, Louisiana). Room has been made in the facilities for additional interferometers, though cost is likely to limit the number that can actually be installed. If a total of 4 interferometers can be used in the LIGO facilities, it may be worthwhile to reconfigure one of the broad-band detectors as a narrow-band instrument in order to search for merger waves, assuming the loss of a broad-band detector would not seriously impact other science goals (e.g., if other detectors worldwide are able to fill the gap).

Second, we strongly advocate continued theoretical efforts to model and understand the properties of merger waves. Of particular interest are robust characteristics such as spectral breaks and features that should be measurable

without needing detailed models of the waves' phasing. This kind of understanding will make it possible to choose a parameterization of the waves, similar to our parameter λ , that leaves a strong mark on the waveform and can be measured reasonably well. A robust theoretical foundation for the merger waves will make it possible to choose our priors and configure our network usefully so that measurements will teach us about the merger waves relatively quickly.

As we have repeatedly emphasized, this analysis should be considered a first, proof-of-concept presentation of how network tuning can work. We believe it is very important that, having presented the principles and a simple example of how they work, this effort be followed by a detailed followup analysis that uses a description of the waves and the detectors that is more sophisticated than our toy model. In wave modeling, we must investigate merger waveforms that are not as trivially simple as those used in the toy model. In principle, this is not too difficult even now — some groups have already produced examples of merger waves that show the influence of the dense matter EOS [11, 12]. Those waveforms could be built into this analysis without too much difficulty.

In the detector description, it is very important that the true bandwidth behavior of the narrow-band interferometers be included — our infinitesimal bandwidth description is clearly inadequate. Real detectors will be far more complicated than the toy description given here, and many of these complications are actually coupled (for example, changing the center frequency of a narrow-band detector impacts its bandwidth). A realistic assessment of how well network tuning can work and how it should be implemented must take into account these various coupled complications. It would also be useful to include acoustic narrow-band detectors in this analysis [21], in order to assess what role they could play in concert with the broad-band interferometric detectors.

It would not be too surprising if including a non-zero bandwidth detector in this description improved the performance of network tuning — finite bandwidth detectors will sample a moderate span of frequency, and can thus look for merger power more broadly than do the toy detectors considered here. This comes at a bit of cost: the broader the bandwidth of the detector, the less amplitude sensitivity it has at its center frequency. A combination of very narrow-band and moderately narrow-band detectors may turn out to provide the best of both worlds. It would also be interesting to explore how well dynamical tuning might work: if it is possible to detect an inspiral in real time (plausible for strong sources measured in advanced detectors), we may be able to adjust the center frequency of the narrow-band interferometer to follow the gravitational waves as they evolve through the late inspiral and merger. This could significantly speed up convergence of the parameter distributions.

Other simplifications that we have used here should also be removed in a follow-up analysis. In particular, in simulating a sequence of measurements we have assumed that all measurements are at some fixed SNR. This is obviously incorrect. In setting the measured SNR, it would be more appropriate to assume a uniform distribution in volume out to some distance (say 500 Mpc), and to set the distance to each source according to that distribution. Then, each measured event should have its angular function Ψ [defined in the text following Eq. (3.16)] taken from the appropriate distribution (cf. Ref. [18]). Also, when we construct the posterior distribution following a simulated measurement, it would be much more appropriate to construct a noise instance \vec{n} and hence simulate the data stream \vec{g} , rather than ensemble averaging.

We advocate undertaking this kind of follow-up analysis soon, so that these algorithms are well-understood when it become possible to actually construct the relevant detector networks, and so that what is learned from them can impact the design of future detectors.

Acknowledgments

I thank Kip Thorne, who played an instrumental role in helping to develop the major ideas that lie at the core of this analysis, and also offered helpful comments and criticism. I am also very grateful to Krishna Rajagopal for useful comments on a draft of this paper, and to Gregg Harry and David Shoemaker for adding much-needed experimental realism to an ignorant theorist's utopian ideas. An early version of these ideas was first presented in Chapter 4 of the author's Ph. D. thesis (Ref. [32]), which was supported by NSF Grant PHY-9424337 at Caltech. This work was supported at the KITP by NSF Grant PHY-9907949.

APPENDIX A: EVALUATION OF THE INTEGRAL (2.7)

In this appendix, we evaluate the integral (2.7), and thereby calculate the posterior probability distribution $P_{\text{post}}(\lambda|\hat{\lambda})$. First, consider a single detector: the posterior probability in this case is

$$P_{\text{post}}(\lambda|\hat{\lambda}) = \mathcal{K} p_0(\lambda) \int \exp \left[-\frac{1}{2} (n|n) \right] \exp \left[-\frac{1}{2} (\delta h|\delta h) - (n|\delta h) - \frac{1}{2} (n|n) \right] \mathcal{D}n, \quad (\text{A1})$$

where the “one-detector” inner product is

$$(a|b) = 4 \operatorname{Re} \int_0^\infty \frac{\tilde{a}(f)^* \tilde{b}(f)}{S_h(f)} df . \quad (\text{A2})$$

Following Finn [17], we evaluate the functional integral (A1) by treating the datastream in the limit of discrete sampling. Take the total span of data to be of finite duration T . Let the sampling time be Δt , and define

$$\begin{aligned} t_i &= i\Delta t, & i &= 0, \dots, \mathcal{N}, \\ a_i &= a(t_i), \\ C_{n,ij} &= C_n(t_i - t_j). \end{aligned} \quad (\text{A3})$$

The function $C_n(t)$ is the noise autocorrelation,

$$C_n(\tau) = \operatorname{E}\{n(t)n(t+\tau)\}_n, \quad (\text{A4})$$

related to the spectral density by

$$S_h(f) = 2 \int_{-\infty}^\infty e^{2\pi i f \tau} C_n(\tau) d\tau . \quad (\text{A5})$$

Let \mathbf{a} be the vector whose components are a_i , and let \mathbf{C}_n be the matrix whose components are $C_{n,ij}$. Note that \mathbf{C}_n is a real, symmetric matrix. The inner product (A2) becomes [cf. [17], Eq. (2.20)]

$$(a|b) = \lim_{\substack{\Delta t \rightarrow 0 \\ T \rightarrow \infty}} \mathbf{a} \cdot \mathbf{C}_n^{-1} \cdot \mathbf{b} . \quad (\text{A6})$$

The probability distribution (A1) can therefore be written

$$P_{\text{post}}(\lambda|\hat{\lambda}) = \lim_{\substack{\Delta t \rightarrow 0 \\ T \rightarrow \infty}} p_0(\lambda) \int \exp \left[-\mathbf{n} \cdot \mathbf{C}_n^{-1} \cdot \mathbf{n} - \mathbf{n} \cdot \mathbf{C}_n^{-1} \cdot \delta \mathbf{h} - \frac{1}{2} \delta \mathbf{h} \cdot \mathbf{C}_n^{-1} \cdot \delta \mathbf{h} \right] d\mathbf{n} . \quad (\text{A7})$$

This integral is of a form commonly encountered in path integral quantization, and evaluates to

$$\begin{aligned} P_{\text{post}}(\lambda|\hat{\lambda}) &= \lim_{\substack{\Delta t \rightarrow 0 \\ T \rightarrow \infty}} p_0(\lambda) \exp \left[-\frac{1}{4} \delta \mathbf{h} \cdot \mathbf{C}_n^{-1} \cdot \delta \mathbf{h} \right] \\ &= p_0(\lambda) \exp \left[-\frac{1}{4} (\delta h | \delta h) \right] . \end{aligned} \quad (\text{A8})$$

[We have absorbed a constant proportional to $1/\sqrt{\det \mathbf{C}_n}$ into the prior probability $p_0(\lambda)$.]

Now consider the entire detector network:

$$P_{\text{post}}(\lambda|\hat{\lambda}) = \mathcal{K} p_0(\lambda) \int \exp \left[-\frac{1}{2} (\vec{n} | \vec{n}) \right] \exp \left[-\frac{1}{2} (\delta \vec{h} | \delta \vec{h}) - (\vec{n} | \delta \vec{h}) - \frac{1}{2} (\vec{n} | \vec{n}) \right] \mathcal{D}\vec{n} . \quad (\text{A9})$$

Recall that the “network” inner product is

$$(\vec{a} | \vec{b}) \equiv 4 \operatorname{Re} \int_0^\infty df \tilde{a}_i(f)^* [\mathbf{S}_h(f)^{-1}]^{ij} \tilde{b}_j(f) . \quad (\text{A10})$$

Because the matrix $\mathbf{S}_h(f)^{-1}$ is real and symmetric, its eigenvectors are orthonormal. If the matrix of eigenvectors is \mathbf{A} then $\mathbf{A}^{-1} = \mathbf{A}^T$, and the matrix

$$\mathbf{Z}_h(f)^{-1} = \mathbf{A} \cdot \mathbf{S}_h(f)^{-1} \cdot \mathbf{A}^T \quad (\text{A11})$$

is diagonal. Define further

$$\begin{aligned} \tilde{a}'_j(f)^* &= \tilde{a}_i(f)^* A_j^i, \\ \tilde{b}'_j(f) &= A_j^i \tilde{b}_i(f). \end{aligned} \quad (\text{A12})$$

Using Eqs. (A11) and (A12), the inner product becomes

$$\begin{aligned}
\langle \vec{a} | \vec{b} \rangle &= 4 \operatorname{Re} \int_0^\infty \tilde{a}_n(f)^* A_k^n A_i^k [\mathbf{S}_h(f)^{-1}]^{ij} A_j^l A_l^m \tilde{b}_m(f) df \\
&= 4 \operatorname{Re} \int_0^\infty \tilde{a}'_k(f)^* [\mathbf{Z}_h^{-1}(f)]^{kl} \tilde{b}'_l(f) df \\
&= \sum_k 4 \operatorname{Re} \int_0^\infty \tilde{a}'_k(f)^* [\mathbf{Z}_h^{-1}(f)]^{kk} \tilde{b}'_k(f) df \\
&\equiv \sum_k \langle a'_k | b'_k \rangle_k .
\end{aligned} \tag{A13}$$

The third equality follows from the fact that $\mathbf{Z}_h^{-1}(f)$ is diagonal. The inner product $\langle a'_k | b'_k \rangle_k$ is identical to the inner product (A2) except that $[\mathbf{Z}_h^{-1}]^{kk}$ is used in place of $1/S_h(f)$. Using (A13), Eq. (A9) becomes

$$\begin{aligned}
P_{\text{post}}(\lambda | \hat{\lambda}) &= \mathcal{K} p_0(\lambda) \int \exp \left[- \sum_k \left(\frac{1}{2} \langle \delta h'_k | \delta h'_k \rangle_k + \langle n'_k | \delta h'_k \rangle_k + \langle n'_k | n'_k \rangle_k \right) \right] \mathcal{D} \vec{n}' \\
&= \mathcal{K} p_0(\lambda) \prod_k \int \exp \left[- \frac{1}{2} \langle \delta h'_k | \delta h'_k \rangle_k - \langle n'_k | \delta h'_k \rangle_k - \langle n'_k | n'_k \rangle_k \right] \mathcal{D} n'_k .
\end{aligned} \tag{A14}$$

Since the matrix \mathbf{A} is unitary, the functional differential element $\mathcal{D} \vec{n}' = \mathcal{D} \vec{n}$. The integral on the last line of (A14) is identical to the integral in Eq. (A1), except for the slightly different inner product. The result is therefore

$$\begin{aligned}
P_{\text{post}}(\lambda | \hat{\lambda}) &= \mathcal{K} p_0(\lambda) \prod_k \exp \left[- \frac{1}{4} \langle \delta h'_k | \delta h'_k \rangle_k \right] \\
&= \mathcal{K} p_0(\lambda) \exp \left[- \frac{1}{4} \sum_k \langle \delta h'_k | \delta h'_k \rangle_k \right] \\
&= \mathcal{K} p_0(\lambda) \exp \left[- \frac{1}{4} (\delta \vec{h} | \delta \vec{h}) \right] .
\end{aligned} \tag{A15}$$

This is the result claimed in Eq. (2.8).

-
- [1] J. P. A. Clark and D. M. Eardley, *Astrophys. J.* **215**, 311 (1977).
 - [2] K. S. Thorne, in *Three Hundred Years of Gravitation*, edited by S. Hawking and W. Israel (Cambridge University Press, Cambridge, England, 1987), p. 330.
 - [3] C. Cutler et al., *Phys. Rev. Lett.* **70**, 2984 (1993).
 - [4] M. Vallisneri, *Phys. Rev. Lett.* **84**, 3519 (2000).
 - [5] See <http://www.ligo.caltech.edu> and links therein for a discussion of the current state of LIGO.
 - [6] D. Kennefick, D. Laurence, and K. S. Thorne, in *Proceedings of the 7th Marcel Grossman Meeting*, edited by R. T. Jantzen and G. Mac Keiser (World Scientific, Singapore, 1997), p. 1090.
 - [7] L. Lindblom, *Astrophys. J.* **398**, 569 (1992).
 - [8] M. Alford, *Lect. Notes Phys.* **583**, 81 (2002).
 - [9] M. G. Alford, K. Rajagopal, S. Reddy, and F. Wilczek, *Phys. Rev. D* **64**, 073017 (2001).
 - [10] X. Zhuge, J. M. Centrella, and S. L. W. McMillan, *Phys. Rev. D* **50**, 6247 (1994); **54**, 7261 (1996).
 - [11] F. A. Rasio and S. L. Shapiro, *Class. Quantum Grav.* **16**, R1 (1999).
 - [12] J. A. Faber, P. Grandclément, F. A. Rasio, and K. Taniguchi, *Phys. Rev. Lett.*, submitted; also astro-ph/0204397.
 - [13] D. G. Blair, *Class. Quantum Grav.* **18**, 4087 (2001).
 - [14] M. Cerdonio, *Class. Quantum Grav.* **18**, 4101 (2001).
 - [15] B. J. Meers, *Phys. Rev. D* **38**, 2317 (1988).
 - [16] J. Mizuno, K. A. Strain, P. G. Nelson, J. M. Chen, R. Schilling, A. Rüdiger, W. Winkler, and K. Danzmann, *Phys. Lett. A* **175**, 273 (1993).
 - [17] L. S. Finn, *Phys. Rev. D* **46**, 5236 (1992).
 - [18] L. S. Finn and D. F. Chernoff, *Phys. Rev. D* **47**, 2198 (1993).
 - [19] C. Cutler and E. E. Flanagan, *Phys. Rev. D* **49**, 2658 (1994).

N_N	$\rho_{\text{insp}} = 10$	$\rho_{\text{insp}} = 30$	$\rho_{\text{insp}} = 90$
1	$f_1 = 630$ Hz	$f_1 = 710$ Hz	$f_1 = 1380$ Hz
2	$f_1 = 620$ Hz, $f_2 = 670$ Hz	$f_1 = 620$ Hz, $f_2 = 780$ Hz	$f_1 = 760$ Hz, $f_2 = 1390$ Hz
3	$f_1 = 600$ Hz, $f_2 = 660$ Hz, $f_3 = 700$ Hz	$f_1 = 590$ Hz, $f_2 = 690$ Hz, $f_3 = 820$ Hz	$f_1 = 740$ Hz, $f_2 = 1340$ Hz, $f_3 = 1420$ Hz
4	$f_1 = 590$ Hz, $f_2 = 650$ Hz, $f_3 = 700$ Hz, $f_4 = 730$ Hz	$f_1 = 580$ Hz, $f_2 = 670$ Hz, $f_3 = 790$ Hz, $f_4 = 1390$ Hz	$f_1 = 650$ Hz, $f_2 = 770$ Hz, $f_3 = 1350$ Hz, $f_4 = 1430$ Hz
5	$f_1 = 580$ Hz, $f_2 = 630$ Hz, $f_3 = 680$ Hz, $f_4 = 710$ Hz, $f_5 = 740$ Hz	$f_1 = 580$ Hz, $f_2 = 660$ Hz, $f_3 = 780$ Hz, $f_4 = 1350$ Hz, $f_5 = 1400$ Hz	$f_1 = 660$ Hz, $f_2 = 760$ Hz, $f_3 = 1320$ Hz, $f_4 = 1400$ Hz, $f_5 = 1450$ Hz

TABLE I: Optimal detector networks in the toy description for uniform prior probability distribution. This table shows the central frequencies for networks with one broad-band and N_N narrow-band detectors, for several values of inspiral SNR.

- [20] E. Gustafson, D. Shoemaker, K. Strain, and R. Weiss, *LSC White Paper on Detector Research and Development*, LIGO Project Document T990080-00-D (1999).
- [21] G. M. Harry, J. L. Houser, and K. A. Strain, *Phys. Rev. D* **65**, 082001 (2002).
- [22] E. Poisson and C. M. Will, *Phys. Rev. D* **52**, 848 (1995).
- [23] E. E. Flanagan and S. A. Hughes, *Phys. Rev. D* **57**, 4566 (1998).
- [24] K. Belczynski, V. Kalogera, and T. Bulik, *Astrophys. J.* **572**, 407 (2001).
- [25] C. Kim, V. Kalogera, and D. R. Lorimer, *Astrophys. J.*, submitted (astro-ph/0207408).
- [26] The program BENCH can be obtained from the URL <http://gravity.phys.psu.edu/Bench>
- [27] A. Królak, J. A. Lobo, and B. Meers, *Phys. Rev. D* **43**, 2470 (1991).
- [28] A. Królak, *Acta Cosmologica* **22-1**, 1 (1996).
- [29] D. Shoemaker, private communication.
- [30] A. Buonanno and Y. Chen, *Class. Quantum Grav.* **18**, L95 (2001).
- [31] W. H. Press, S. A. Teukolsky, W. T. Vetterling, and B. P. Flannery, *Numerical Recipes* (Cambridge University Press, Cambridge, 1992).
- [32] S. A. Hughes, unpublished Ph. D. thesis, Caltech, 1998.

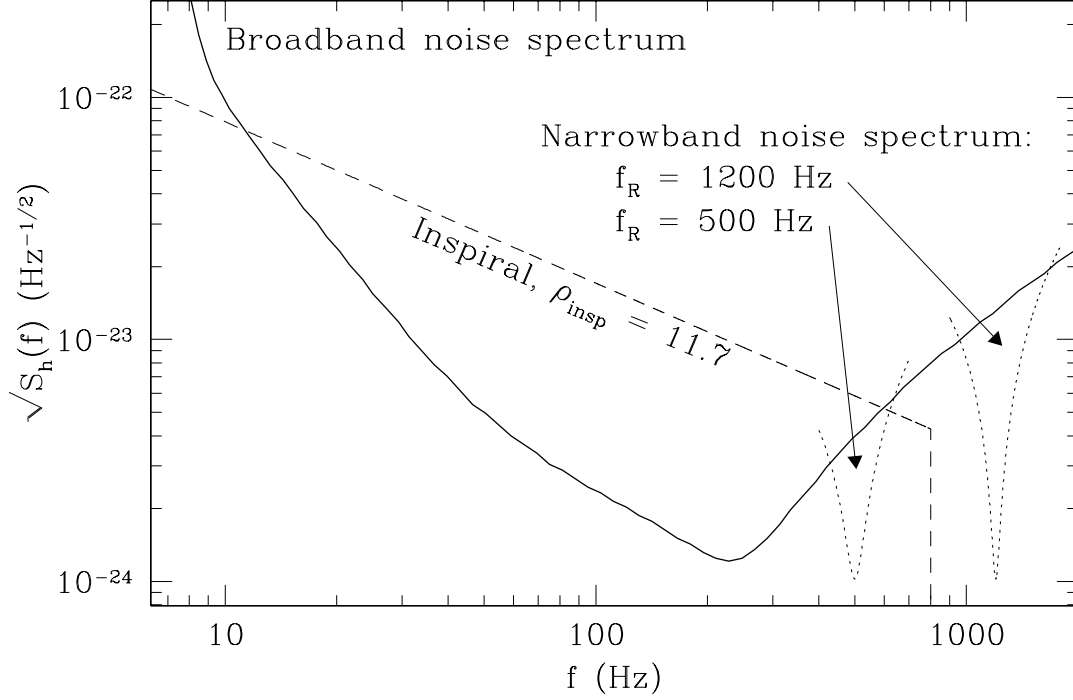


FIG. 1: Broad-band noise used in this analysis (second generation LIGO sensitivity, optimized to detect binary neutron star inspiral), with two examples of narrow-band interferometer noise. These examples are for resonant frequencies of 500 Hz and 1200 Hz; each assumes a bandwidth of 50 Hz. The dashed line is a representation of the wave strain for a signal whose inspiral SNR is 11.7 (corresponding to an optimally oriented source at 500 Mpc, or an “average” source at 200 Mpc).

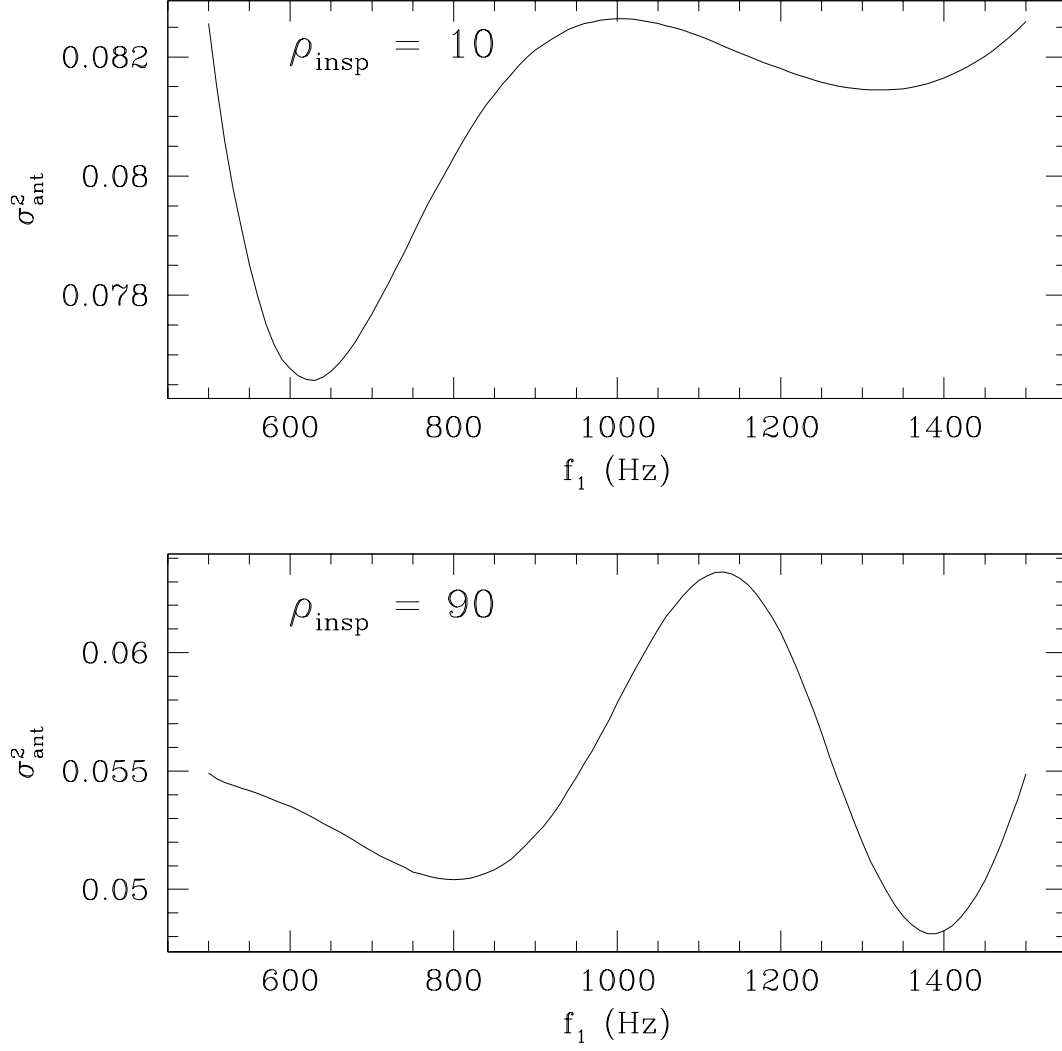


FIG. 2: The anticipated variance for measurements with a single narrow-band detector at inspiral SNR $\rho_{\text{insp}} = 10$ and $\rho_{\text{insp}} = 90$. At relatively low SNR, the tuning algorithm places the narrow-band detector at $f \simeq 620$ Hz to avoid false positives, since it knows the signal will be extremely weak at high frequencies. At high SNR, the algorithm places the detector at $f \simeq 1400$ Hz — the risk of a false positive is much lower, so the algorithm chooses the narrow-band detector to counter the rapidly growing broad-band noise.

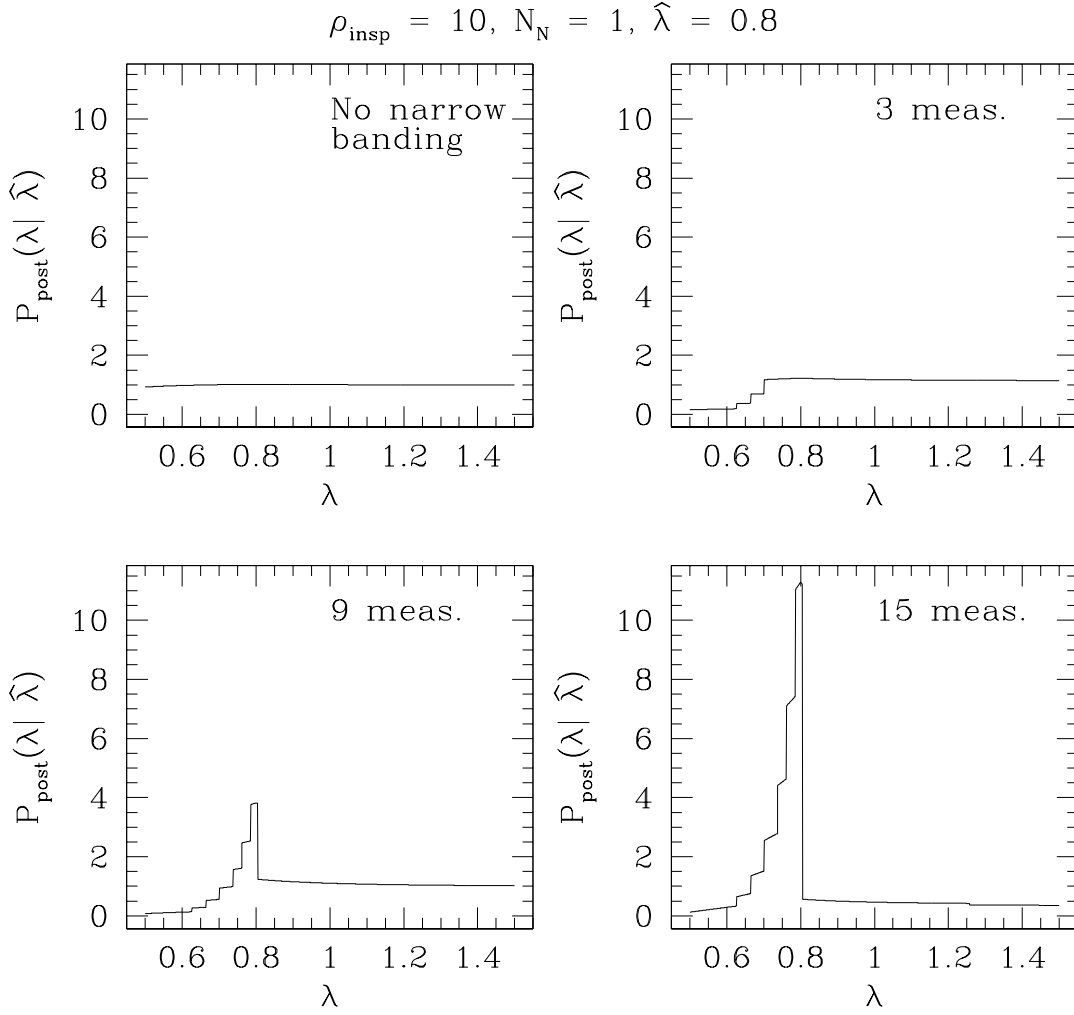


FIG. 3: The evolution of the posterior probability distribution, measuring coalescences with $\rho_{\text{insp}} = 10$, $\hat{\lambda} = 0.8$, and a single narrow-band detector. After each measurement, we update the prior distribution, $p_0^i(\lambda) = P_{\text{post}}^{i-1}(\lambda | \hat{\lambda})$, and then retune the network (minimizing σ_{ant}^2). In this way, multiple measurements drive the network to “zoom in” on a distribution that is peaked about the true value $\hat{\lambda}$. In the case shown here, the distribution starts to become peaked after about 9 measurements, and has a pronounced peak after 15 measurements.

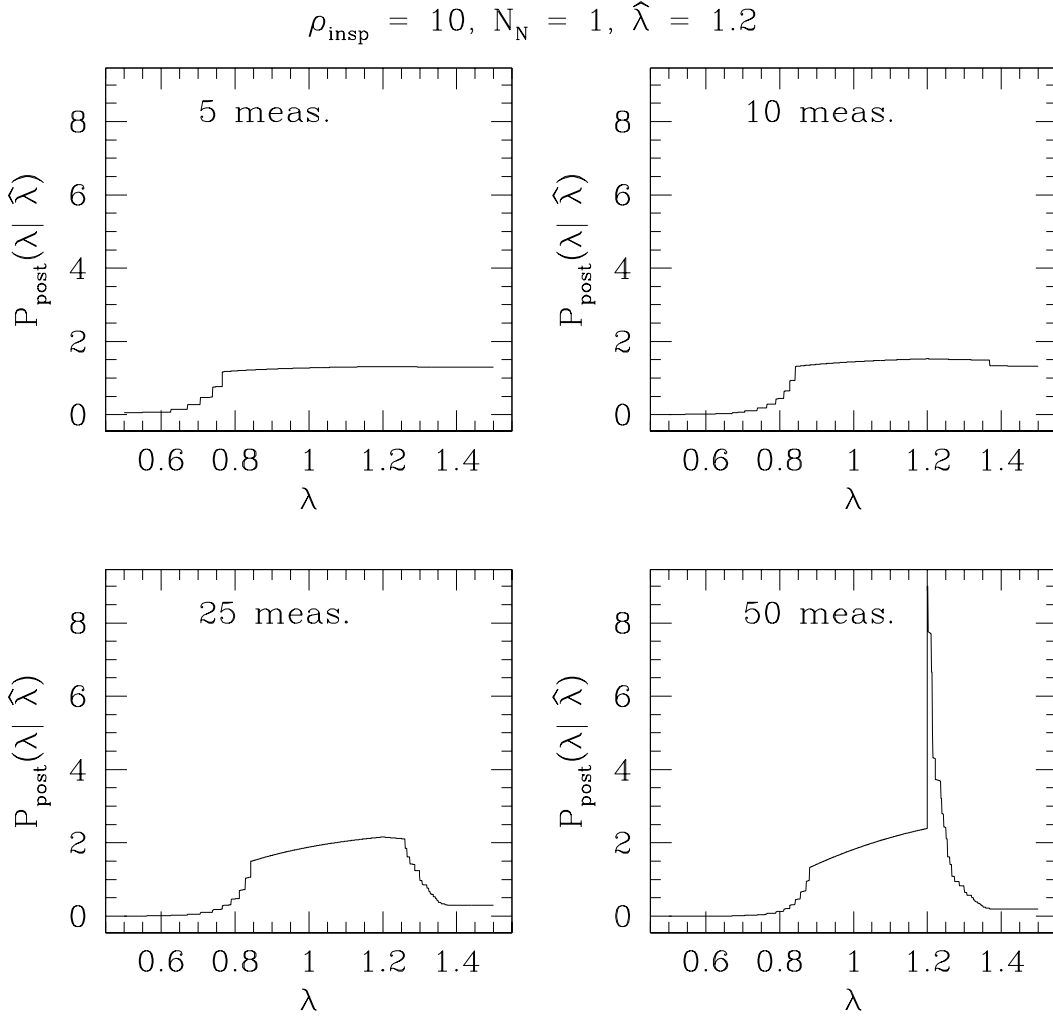


FIG. 4: The same as Fig. 3, but with $\hat{\lambda} = 1.2$. The evolution of the posterior probability is qualitatively similar to the evolution when $\hat{\lambda} = 0.8$, but is much slower. At this signal strength, the tuning algorithm tends not to sample the high-frequency end of its parameter space, in order to reduce the probability of false positive measurements. Because the merger occurs at high frequency in this case, the algorithm takes quite a while to find the merger power.

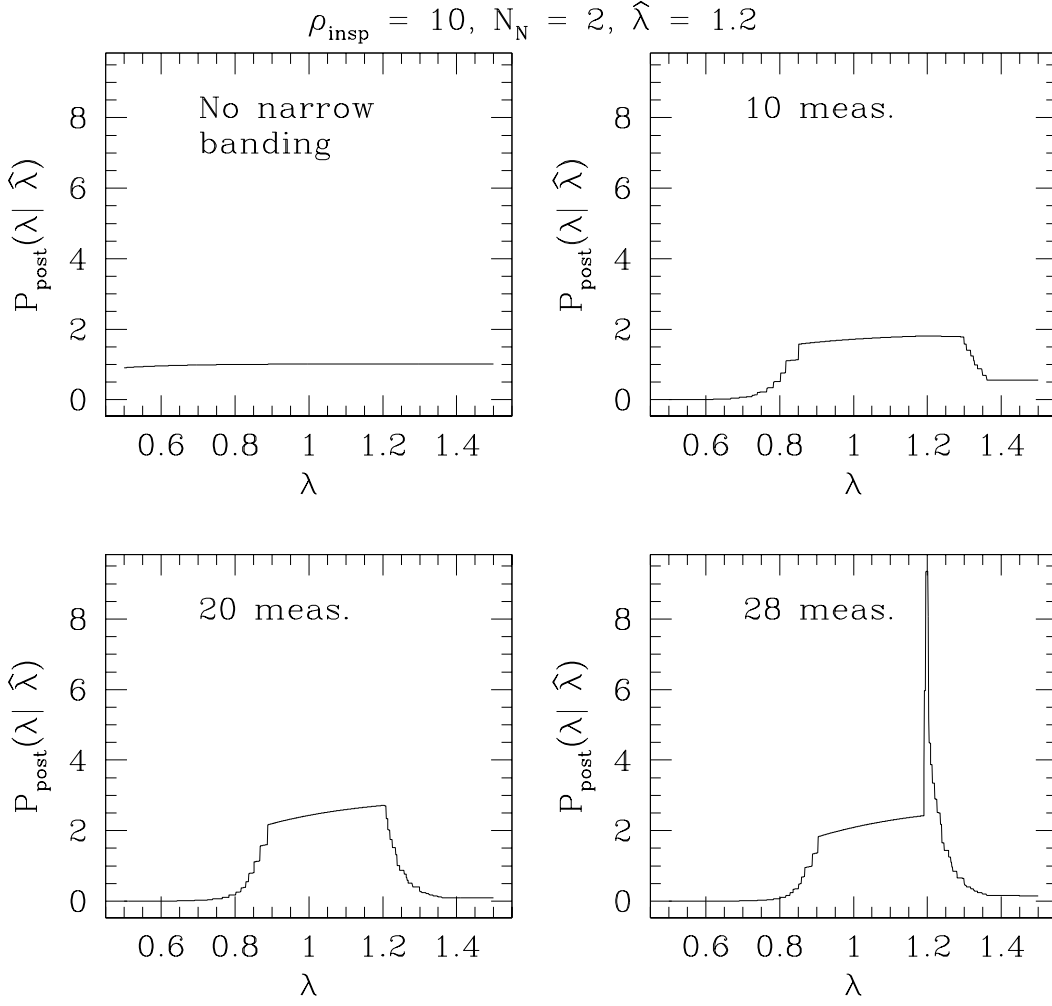


FIG. 5: The same as Fig. 4, but using two narrow-band detectors. Convergence onto a distribution peaked near $\hat{\lambda}$ is still slow, but not as bad as when a single detector is used.

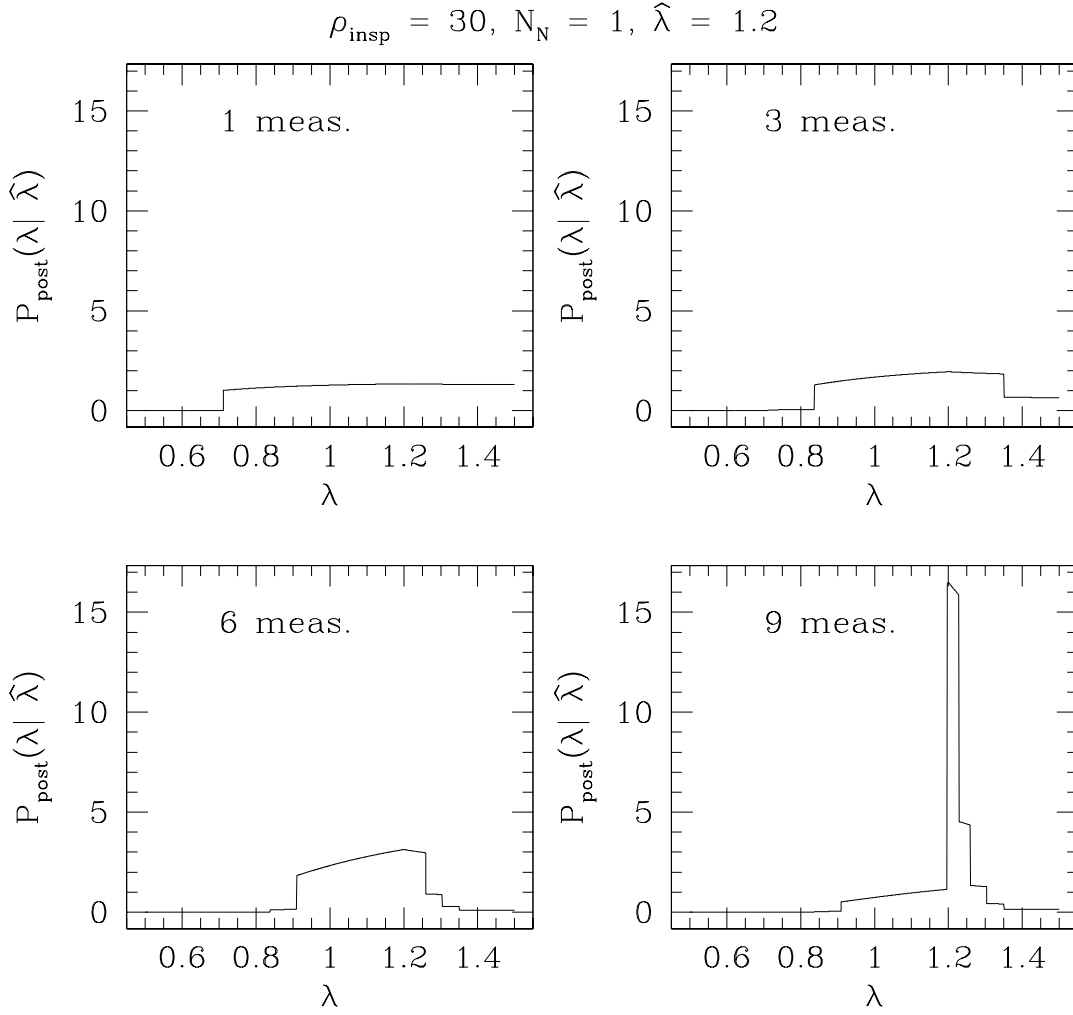


FIG. 6: The same as Fig. 4, but at higher SNR: $\rho_{\text{insp}} = 30$. SNR has a marked effect on the rate at which the distributions converge onto $\hat{\lambda}$. The algorithm does not need to worry about false positives so much in this case, and so it is quite happy to assign the single detector to high frequencies when necessary. As a consequence, the distribution is quite peaked after only 9 measurements — in marked contrast to the 50 measurements needed when $\rho_{\text{insp}} = 10$.